



Enhanced charge transfer kinetics of $\text{Fe}_2\text{O}_3/\text{CdS}$ composite nanorod arrays using cobalt-phosphate as cocatalyst

Panyong Kuang^a, Liuyang Zhang^a, Bei Cheng^a, Jiaguo Yu^{a,b,*}

^a State Key Laboratory of Advanced Technology for Materials Synthesis and Processing, Wuhan University of Technology, Wuhan 430070, PR China

^b Department of Physics, Faculty of Science, King Abdulaziz University, Jeddah 21589, Saudi Arabia

ARTICLE INFO

Article history:

Received 22 April 2017

Received in revised form 29 June 2017

Accepted 1 July 2017

Available online 3 July 2017

Keywords:

Photoelectrochemical water splitting

$\text{Fe}_2\text{O}_3/\text{CdS}/\text{Co-Pi}$ NRAs

Charge transfer kinetics

Photocurrent density

Onset potential

ABSTRACT

Photoelectrochemical (PEC) water splitting is one of the most efficient strategies to meet the challenges of the global energy crisis. Although hematite ($\alpha\text{-Fe}_2\text{O}_3$) is a suitable material for PEC, its performance is limited by passive surface state and slow charge transfer kinetics. Here, a successful design and fabrication of novel ternary $\text{Fe}_2\text{O}_3/\text{CdS}/\text{Co-Pi}$ nanorod arrays (NRAs) photoanode is reported aimed at boosting charge separation and transfer kinetics within the bulk and at the electrode/electrolyte interface. As expected, the results reveal that $\alpha\text{-Fe}_2\text{O}_3$ sluggish reaction kinetics is greatly ameliorated upon depositing CdS and Co-Pi, and surface charge recombination decreases even more, resulting in substantially enhanced photocurrent density. Moreover, noticeable onset potential negative shift evidenced by the $I\text{-}V$ curve is found to result from the deposition of CdS and Co-Pi, which allows the ternary composite to generate photocurrent at much lower applied potential. We elaborate the synergistic effect of CdS and Co-Pi in achieving faster charge transfer kinetics and lower onset potential for photocurrent. These results provide new insights into the surface reaction kinetics of Co-Pi/semiconductor photoanode toward PEC application.

© 2017 Elsevier B.V. All rights reserved.

1. Introduction

Photoelectrochemical (PEC) water splitting, which converts solar energy into clean hydrogen and oxygen fuel, has attracted world-wide attention as a solution to the global energy crisis. One of the primary components of the PEC cell is the semiconductor photoelectrode [1,2]. To date, oxide semiconductor-based photoelectrodes such as $\alpha\text{-Fe}_2\text{O}_3$ [3,4], ZnO [5,6], TiO₂ [7,8] and BiVO₄ [9,10] have been extensively investigated and optimized in PEC water splitting applications due to their great potential for efficient solar energy conversion. Among these oxides, hematite ($\alpha\text{-Fe}_2\text{O}_3$) is one of the widely used photoanode materials due to its favorable optical band gap (~2.0 eV) [11], a sufficiently positive valence band position for water oxidation [12] and outstanding chemical stability in alkaline electrolytes [13]. Theoretical study reveals that $\alpha\text{-Fe}_2\text{O}_3$ can achieve a high maximum solar-to-hydrogen efficiency of 16.8% under AM 1.5G illumination due to its narrow band gap [14]. However, the experimental water splitting efficiency is far below the

theoretical value and this has been attributed to sluggish water oxidation kinetics [15], low carrier mobility (<1 cm² V⁻¹ S⁻¹) [16] and short hole diffusion length (~2–4 nm) [17], resulting in serious recombination of charge carriers in Fe_2O_3 .

Generally, two key factors influence the practical PEC performance of Fe_2O_3 : charge separation efficiency and charge transfer efficiency. In this regard, tremendous efforts have been made to improve the charge separation efficiency of Fe_2O_3 , including heterojunction construction [15,18], metal-element doping [19] and oxygen defects creation [20]. Constructing heterojunction is effective because the merits of different semiconductor materials are integrated in one single photoelectrode. It is worth noting that cadmium sulfide (CdS) sensitized one-dimensional metal oxide photoelectrodes have been proven to be an efficient strategy to achieve high charge separation efficiency. Building on the successful ZnO/CdS and TiO₂/CdS photoanode models [21–24], $\text{Fe}_2\text{O}_3/\text{CdS}$ photoanode is predicted to show superior PEC performances due to the visible light response of both Fe_2O_3 and CdS, which significantly extend solar utilization and increase the number of photoinduced electron-hole pairs generated. More importantly, typical type-II mode band-gap structure between Fe_2O_3 and CdS results in effective charge carrier separation and thus suppresses the internal charge recombination caused by the slow carrier transport kinetics of Fe_2O_3 [25,26]. For instance, $\text{Fe}_2\text{O}_3/\text{CdS}$ corn-like

* Corresponding author at: State Key Laboratory of Advanced Technology for Materials Synthesis and Processing, Wuhan University of Technology, Wuhan 430070, PR China.

E-mail addresses: jiaguoyu@yahoo.com, yujiagu93@163.com (J. Yu).

nanorods demonstrated enhanced photocatalytic performance as compared to the pristine Fe_2O_3 and CdS , and this was attributed to the promotion of charge carrier separation at the $\text{Fe}_2\text{O}_3/\text{CdS}$ interface [27]. Zhang et al. synthesized wide spectral responsive three-dimensional $\text{CdS}/\text{Fe}_2\text{O}_3$ heterojunction nanocomposite and this composite exhibited superior photocatalytic reduction activity for Cr(VI) [28]. Despite these achievements in photocatalysis, there are few reports on the use of $\text{Fe}_2\text{O}_3/\text{CdS}$ in PEC water splitting. Notably, even though effective charge carrier separation can be realized by the aforementioned metal oxide/ CdS heterostructured photoanodes, the solar-energy-conversion efficiency is always hindered by the slow charge transfer kinetics, suffering significantly from electron-hole pair recombination within the bulk and at the electrode/electrolyte interface. These problems severely impede practical PEC water splitting application.

To improve the interfacial hole extraction kinetics from the photoanode surface, a simple but earth-abundant, ion-permeable amorphous and self-healing water oxidation cocatalyst cobalt-phosphate (Co-Pi) has attracted some interests recently [29]. Co-Pi stands out in reducing surface kinetic barriers, boosting surface chemical reaction rates and shifting the water oxidation onset potential with ca. 100 – 150 mV in negative direction [30,31]. It still remains disputed how Co-Pi contributes to the performance improvement of a semiconductor. One alternative interpretation proposes that Co-Pi plays the vital role to increase semiconductor band bending near the electrode/electrolyte interface, leading to decreasing surface electron-hole pair recombination and negatively shifted onset potential [32,33]. Co ion can be oxidized to a higher valence state by photoinduced holes, and reverted back to its initial valence state when it oxidizes water molecules or sacrificial agents [34,35]. As the change in valence states of Co is reversible, photoinduced holes accumulated on the photoanode surface are consumed timely and efficiently, the surface charge transfer kinetics could be greatly promoted. To date, many photoanode materials have been modified with Co-Pi, including Ta_3N_5 [36], TaOH [37], TiO_2 [38] and BiVO_4 [39], and all of these heterostructures showed significantly enhanced charge transfer kinetics and reduced onset potential to generate photocurrent. Herein, a novel Co-Pi treated $\text{Fe}_2\text{O}_3/\text{CdS}$ nanorod arrays (NRAs) photoanode has been fabricated. To the best of our knowledge, the fabrication as well as the PEC application of this unique structure is pioneered in this work. Encouragingly, this ternary photoanode greatly improves the charge transfer kinetics due to the synergistic effect of CdS and Co-Pi. Firstly, CdS serves as a light absorber, increasing the light absorption and generation of photoinduced electron-hole pairs. Besides, the typical type-II model band structure of $\text{Fe}_2\text{O}_3/\text{CdS}$ leads to enhanced charge separation efficiency and transfer kinetics, resulting in the inhibition of bulk charge recombination. Secondly, Co-Pi deposited on the $\text{Fe}_2\text{O}_3/\text{CdS}$ accelerates the injection of the separated holes from the electrode to electrolyte and inhibits the hole accumulation at electrode surface, thus resulting in the enhanced surface charge transfer kinetics and reduced onset potential for photocurrent. Last but not least, unlike the general morphologies (nanoparticle, nanoplate), Fe_2O_3 nanorod with vertical geometry structure provides continuous and unimpeded pathways for electron transfer to the external circuit, which also improves charge transfer kinetics and reduces the surface charge recombination. It needs to be emphasized that the charge transfer at electrode/electrolyte interface is the decisive parameter in $\text{Fe}_2\text{O}_3/\text{CdS}/\text{Co-Pi}$ photoanode during PEC process, as verified by electrochemical impedance spectroscopy (EIS). In other words, the introduction of Co-Pi has greatly supported the efficient hole transfer and consumption against the unproductive and energy-wasted surface electron-hole recombination to achieve improved charge transfer kinetics and lower onset potential. To

sum up, this ternary composite pattern opens up new insight for photoelectrode surface state modification toward PEC application.

2. Experimental

2.1. Sample preparation

Sinopharm Chemical Reagent Co., Ltd. (Shanghai, China) supplied analytical grade $\text{FeCl}_3 \cdot 6\text{H}_2\text{O}$, $\text{CO}(\text{NH}_2)_2$ (urea), $\text{Cd}(\text{NO}_3)_2 \cdot 4\text{H}_2\text{O}$, $\text{CN}_2\text{H}_4\text{S}$ (thiourea), $\text{Na}_3\text{C}_6\text{H}_5\text{O}_7 \cdot 2\text{H}_2\text{O}$ (trisodium citrate), $\text{NH}_3 \cdot \text{H}_2\text{O}$ (ammonia), $\text{Na}_2\text{HPO}_4 \cdot 12\text{H}_2\text{O}$, $\text{NaH}_2\text{PO}_4 \cdot 2\text{H}_2\text{O}$ and $\text{Co}(\text{NO}_3)_2 \cdot 6\text{H}_2\text{O}$. For sample synthesis, these reagents are used directly without further purification.

Fe_2O_3 nanorod arrays (NRAs) were synthesized by combining simple and facile hydrothermal method with calcination treatment. Typically, 30 mL of deionized water was measured to dissolve 1.01 g of $\text{FeCl}_3 \cdot 6\text{H}_2\text{O}$ and 0.33 g of urea. A homogeneous solution was formed by continuous stirring for 20 min. Subsequently, the solution was poured into two 25 mL Teflon-lined stainless steel autoclaves equally, and a piece of clean fluorine-doped tin oxide (FTO) glass (2 cm × 1.5 cm) was then immersed into the solution with the conductive surface facing downwards. After hydrothermal treatment at 100 °C for 12 h, the FeOOH NRAs coated FTO glass obtained was washed with deionized water to remove the residual impurities. The dried sample was subsequently annealed at 800 °C in air for a certain time at a heating rate of 15 °C/min to convert the yellow FeOOH to reddish-brown Fe_2O_3 .

$\text{Fe}_2\text{O}_3/\text{CdS}$ NRAs was fabricated by chemical bath deposition (CBD). 0.05 g $\text{Cd}(\text{NO}_3)_2 \cdot 4\text{H}_2\text{O}$, 0.05 g trisodium citrate and 0.01 g thiourea were well-dissolved in 70 mL of distilled water with ultrasonication and stirring for about 20 min. The pH of the aqueous solution was carefully adjusted to around 11 by drop-wise addition of concentrated ammonia solution. The CdS nanoparticles were then deposited onto the surface of Fe_2O_3 NRAs on FTO via CBD at 90 °C for 30 min.

Co-Pi cocatalyst was deposited onto the $\text{Fe}_2\text{O}_3/\text{CdS}$ NRAs by photo-assisted deposition method as described previously [40]. Typically, the sample was first immersed into a 0.1 M sodium phosphate buffer solution with 0.5 mM cobalt nitrate for 15 min and the solution was then illuminated by UV-vis light (300 W Xenon lamp) for 1 h. After deposition, Co-Pi modified $\text{Fe}_2\text{O}_3/\text{CdS}$ NRAs were obtained.

2.2. Characterizations

Rigaku diffractometer (Japan) equipped with monochromatized $\text{Cu K}\alpha$ radiation ($\lambda = 0.15418 \text{ nm}$) was used to perform X-ray diffraction (XRD) measurement. Surface morphology and cross-section view of samples were observed by using a field emission scanning electron microscopy (FE-SEM, JEOL JSM-7500) instrument. Energy-dispersive spectroscopy (EDS) was also examined using the same instrument. The microstructure information of the sample was investigated by using a transmission electron microscope (TEM, JEOL JEM-2100F). X-ray photoelectron spectroscopy (XPS) was performed using a Thermo XPS spectrometer system (ESCALab 250) using $\text{Al K}\alpha$ (1486.6 eV, 150 W) radiation to evaluate the surface compositions and valence states. UV-vis diffuse reflectance spectra (UV-vis DRS) was performed using an UV-vis spectrophotometer (Shimadzu UV-2600, Japan) using BaSO_4 as a reference. Renishaw inVia spectrometer ($\lambda = 633 \text{ nm}$) was used to perform Raman spectroscopy at room temperature.

2.3. Photoelectrochemical performances

An electrochemical workstation (CHI 760E, Shanghai CH Instrument Co., Ltd.) equipped with a tetragonal quartz cell was used

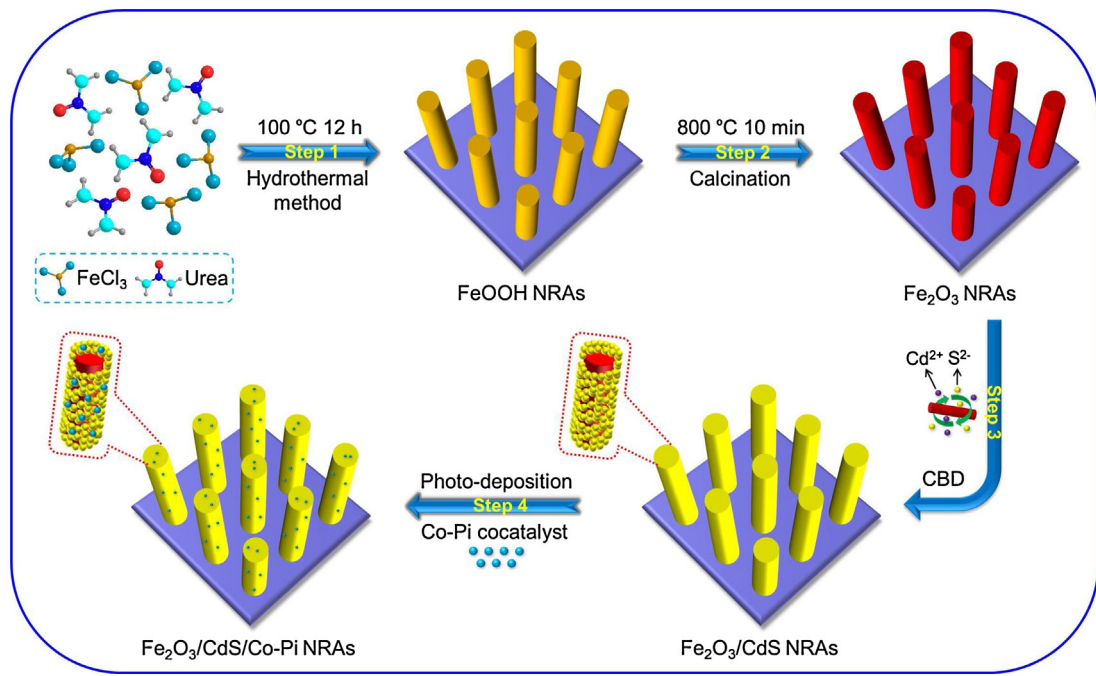


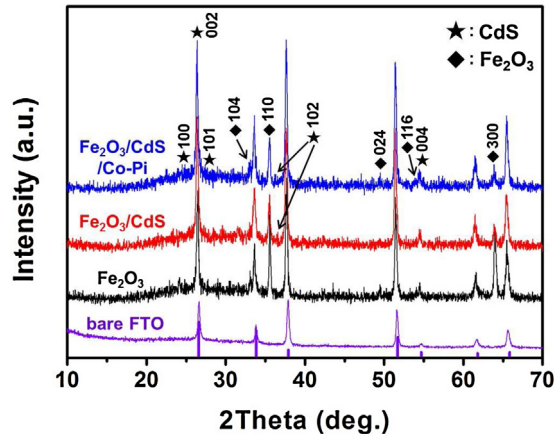
Fig. 1. Schematic illustration of the fabrication processes of $\text{Fe}_2\text{O}_3/\text{CdS}/\text{Co-Pi}$ NRAs.

to evaluate the PEC performances of the samples. The prepared photoanode (working area = 0.25 cm^2), Ag/AgCl electrode and Pt film (1 cm^2) were employed as the working, reference and counter electrode, respectively. $1.0 \text{ M NaOH} + 0.1 \text{ M Na}_2\text{S}$ aqueous solution was adopted as the electrolyte. A 300 W Xenon lamp (Perfect Light Corp. Ltd. Beijing) was used as the light source and radiates incident light with intensity of 100 mW cm^{-2} on the photoelectrode surface. All the I - V curves used in this work have subtracted the dark current without light illumination. The electrode potential (vs. Ag/AgCl) is converted to the Reversible Hydrogen Electrode (RHE) potential according to the Nernst equation [41,42]: $E_{\text{RHE}} = E_{\text{Ag/AgCl}} + 0.059\text{pH} + E^\theta_{\text{Ag/AgCl}}$, where the E_{RHE} is the converted applied potential (vs. RHE), $E_{\text{Ag/AgCl}}$ is the applied potential (vs. Ag/AgCl), and $E^\theta_{\text{Ag/AgCl}}$ is the standard Ag/AgCl electrode potential at 25°C (0.197 V). The pH for the electrolyte is 13.31.

3. Results and discussion

3.1. Phase structure and morphology

As shown in Fig. 1, $\text{Fe}_2\text{O}_3/\text{CdS}/\text{Co-Pi}$ NRAs were prepared through several successive processes including hydrothermal, calcination, CBD and photo-deposition methods. FeOOH NRAs on FTO was first prepared by a simple hydrothermal process (Step 1 in Fig. 1). Fig. S1 shows the morphology, phase and crystal structure of the FeOOH . The nanorods were grown vertically on the substrate with main diameter and length of about 100 nm and 1 μm respectively. After calcination (Step 2), it is found that visible-light-responsive Fe_2O_3 has been converted from FeOOH while retaining the NRAs geometry structure. The photocurrent-potential (I - V) and photocurrent-time (I - T) curves of the pristine Fe_2O_3 NRAs annealed at 650, 750 and 800 $^\circ\text{C}$ were obtained in 1.0 M NaOH under visible light illumination (Fig. S2). Negligible photocurrent is observed for Fe_2O_3 annealed at 650 and 750 $^\circ\text{C}$. However, when the temperature increased to 800 $^\circ\text{C}$, significantly enhanced photocurrent and reduced onset potential can be observed. This photocurrent enhancement could be ascribed to the promoted electron transfer from Fe_2O_3 to FTO substrate, owing to the release of Sn from



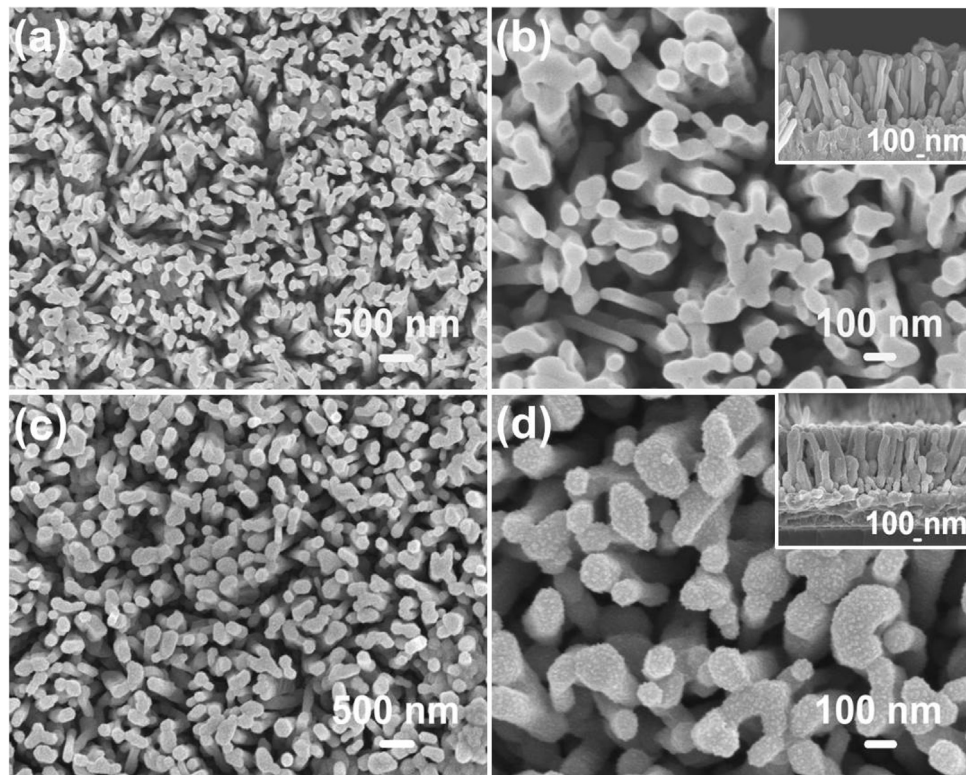


Fig. 3. SEM images of (a,b) pristine Fe_2O_3 and (c,d) $\text{Fe}_2\text{O}_3/\text{CdS}$ NRAs. The inset pictures are cross-section view of NRAs.

XRD pattern of $\text{Fe}_2\text{O}_3/\text{Co-Pi}$ (Fig. S3), no other peaks of Co-Pi can be observed as compared to the XRD pattern of pristine Fe_2O_3 . Meanwhile, the clear evidence of Fe_2O_3 in $\text{Fe}_2\text{O}_3/\text{CdS}/\text{Co-Pi}$ and $\text{Fe}_2\text{O}_3/\text{CdS}$, suggests that the highly ordered NRAs can not only serve as steady support for the deposition of CdS and Co-Pi, but also act as the continuous channel for electron transfer, which is beneficial for the improvement of the charge transfer efficiency and charge carrier lifetime.

The surface morphologies of Fe_2O_3 , $\text{Fe}_2\text{O}_3/\text{CdS}$ and $\text{Fe}_2\text{O}_3/\text{CdS}/\text{Co-Pi}$ NRAs were examined by scanning electron microscopy (SEM). As shown in Fig. 3a–b, the pristine Fe_2O_3 NRAs, with smooth surface and average diameter of about 100 nm, are grown quasi-vertically on the FTO substrate. Cross-section view of the NRAs (Fig. 3b, inset) shows closely aligned nanorods with main length of around 1 μm . After CBD of CdS, the Fe_2O_3 NRAs still maintain their one-dimensional geometry, and most regions of the nanorods are covered with evenly-distributed CdS nanoparticles with average radius of around 10 nm, creating a rough surface (Fig. 3c–d). With the attachment of CdS nanoparticles, the diameter of $\text{Fe}_2\text{O}_3/\text{CdS}$ nanorods becomes greater than 100 nm, whereas the length of $\text{Fe}_2\text{O}_3/\text{CdS}$ remains unchanged (Fig. 3d, inset). Fig. 4a–b display the SEM images of $\text{Fe}_2\text{O}_3/\text{CdS}/\text{Co-Pi}$ NRAs. It is obvious that the surface morphology is changed a little by the photo-deposition and this can be attributed to the slight photo corrosion of CdS. The deposited Co-Pi cocatalyst cannot be distinguished based on morphology and this may be due to the small amount of Co-Pi deposited. However, the existence of Co-Pi can be confirmed from the energy-dispersive spectroscopy (EDS) spectrum (Fig. 4c) as well as the following microstructure and surface composition analysis. Fig. 4d shows the transmission electron microscopy (TEM) image of $\text{Fe}_2\text{O}_3/\text{CdS}/\text{Co-Pi}$ nanorods, and the estimated diameter is consistent with that from SEM images. High-resolution transmission electron microscopy (HRTEM) was carried out to examine the microstructure. As shown in Fig. 4e–g, the lattice fringe spacing is about 0.252 nm, which can be assigned to the

(110) plane of Fe_2O_3 . Moreover, two lattice fringes with spacing of 0.315 and 0.245 nm match well with the (101) and (102) planes of CdS, respectively. Fig. 4h–i display the selected-area electron diffraction (SAED) patterns of Fe_2O_3 and CdS, respectively, which was converted from Fig. 4f–g directly. Notably, compact and continuous interface among Fe_2O_3 , CdS and Co-Pi, as shown in Fig. 4d–e, could facilitate spatial separation and fast transport of charge carriers to achieve superior PEC performances. Fig. 5 shows the element mapping images including O, Fe, Sn, Cd, S, Co and P, which is in agreement with the EDS spectrum. Furthermore, the even distribution of these elements further supports the formation of a ternary nanocomposite.

3.2. XPS analysis

To gain more insight into the surface compositions and valence states of the photoanodes, X-ray photoelectron spectroscopy (XPS) measurement was conducted. Fig. 6a shows the whole range of XPS spectra. Notably, the binding energy of Fe 2p XPS spectrum for $\text{Fe}_2\text{O}_3/\text{CdS}/\text{Co-Pi}$ exhibits a slight right shift compared with that of $\text{Fe}_2\text{O}_3/\text{CdS}$ and Fe_2O_3 (Fig. 6b). This shift is caused by surface modification of Co-Pi according to literature [46]. Fig. 6c presents the Cd 3d XPS spectrum with peaks of $3d_{5/2}$ at around 405.6 eV and $3d_{3/2}$ at 412.3 eV, which indicates the existence of Cd^{2+} in the as-prepared photoanodes [47,48]. Two peaks located at around 161.8 and 162.9 eV in Fig. 6d can be ascribed to S $2p_{3/2}$ and S $2p_{1/2}$, respectively, which are derived from the S^{2-} in Cd-S [49,50]. In the case of Co 2p XPS spectrum (Fig. 6e), the two split peaks centered at around 781.6 and 797.3 eV can be attributed to Co $2p_{3/2}$ and Co $2p_{1/2}$, where the former can be assigned to Co^{2+} and the latter can be ascribed to Co^{3+} , respectively [51,52]. The peak of P 2p XPS spectrum in Fig. 6f centered at around 133.4 eV stems from the phosphate group in Co-Pi cocatalyst [53]. The existence of Co^{3+} in Co-Pi cocatalyst directly indicates that Co^{2+} was partially oxidized into Co^{3+} during the photo-deposition procedure. The ratio

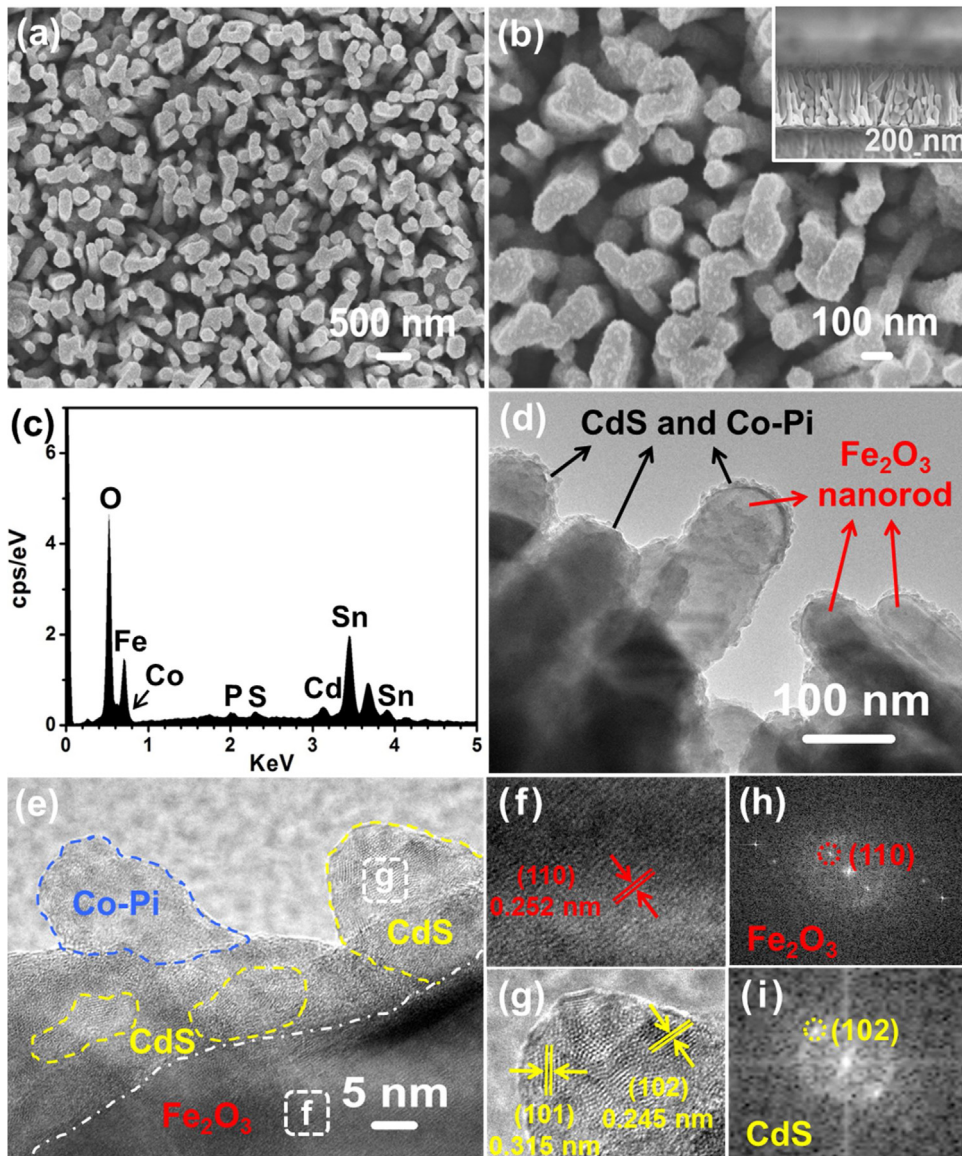


Fig. 4. (a,b) SEM images and (c) EDS spectrum of the $\text{Fe}_2\text{O}_3/\text{CdS}/\text{Co-Pi}$ NRAs, (d) TEM image and (e-g) high-resolution TEM images of $\text{Fe}_2\text{O}_3/\text{CdS}/\text{Co-Pi}$ nanorods, and SAED patterns of (h) Fe_2O_3 and (i) CdS.

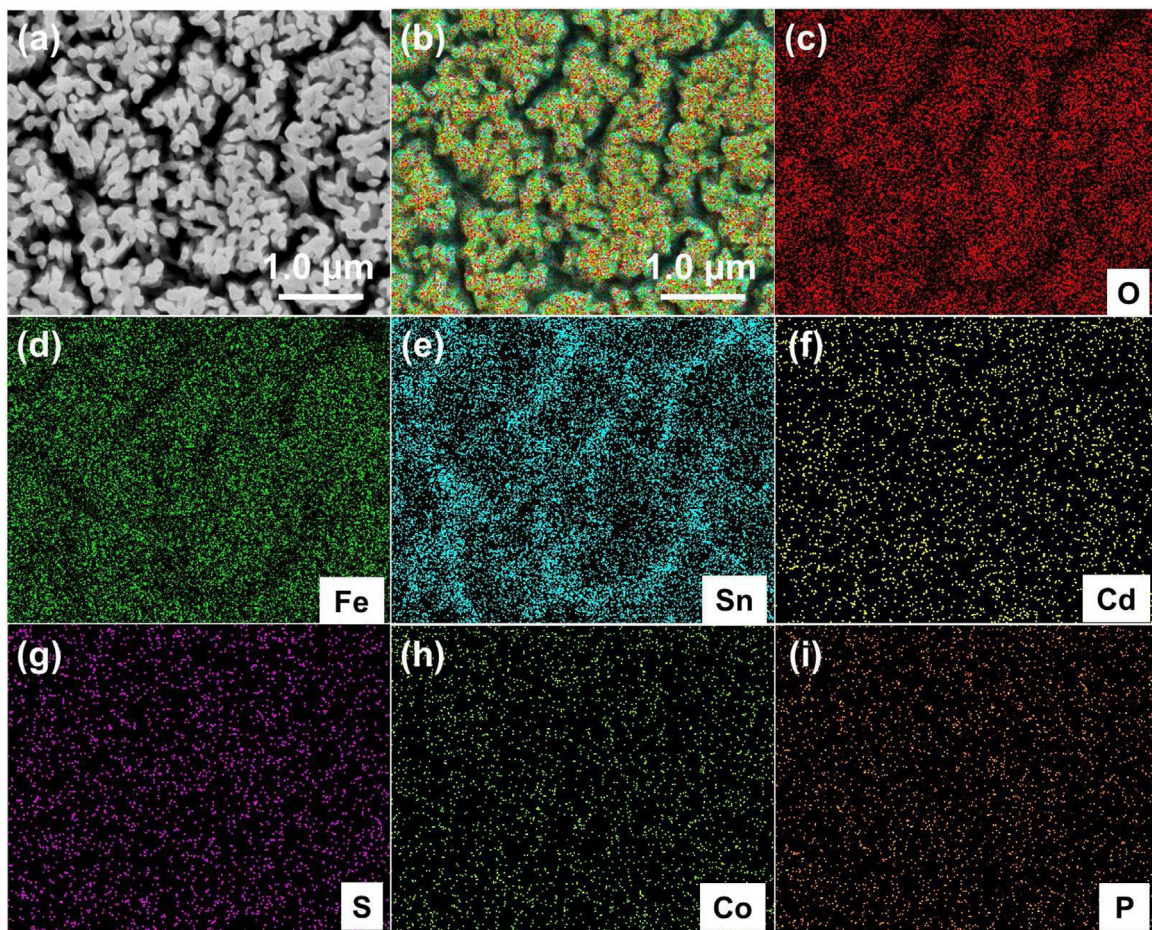
of $\text{Co}^{2+}/\text{Co}^{3+}$ in Co-Pi is not so important because the valence states of Co ions could reversibly alternate during the oxidation reactions. Fig. S4 presents the O 1s XPS spectra of the three samples. The peak centered at around 529.8 eV corresponds to the Fe^{3+} oxide [54], and the peaks located at around 531.2 eV are attributed to the surface-adsorbed oxygen or hydroxyl species [55]. Compared to the XPS spectra of Fe_2O_3 and $\text{Fe}_2\text{O}_3/\text{CdS}$ (Fig. S4a-b), there is a new peak centered at around 532.9 eV for $\text{Fe}_2\text{O}_3/\text{CdS}/\text{Co-Pi}$ XPS spectrum in Fig. S4c, and it can be indexed to the P-O-P bond of phosphate [56], this is in agreement with the P 2p XPS spectrum and further proves the formation of Co-Pi cocatalyst. Therefore, the above analysis demonstrates the successful preparation of chemical-coupling $\text{Fe}_2\text{O}_3/\text{CdS}/\text{Co-Pi}$ NRAs photoanode.

3.3. Raman and UV-vis spectra

Raman spectroscopy was carried out to further analyze the crystal structure (Fig. 7a). Typically, seven major characteristics bands, which are associated with two classes of Raman active optical modes ($2\text{A}_\text{g} + 5\text{E}_\text{g}$) of Fe_2O_3 , can be observed for all three sam-

ples. Five of those peaks at 249, 296, 301, 414 and 615 cm^{-1} are attributed to the vibrations with symmetry E_g , whereas the other two peaks at 229 and 500 cm^{-1} can be assigned to A_g mode of Fe_2O_3 , respectively [57,58]. It is worth noting that the peak at 663 cm^{-1} should be the LO mode of Fe_2O_3 , which is ascribed to the Raman space symmetry breakdown and activation of extra modes induced by lattice defects or short-range order due to a great quantity of surface defects in this nanomaterial [13,59]. These above peaks are all derived from Fe_2O_3 , since no peaks can be observed from the Raman spectrum of bare FTO substrate (Fig. S5).

The comparison of the UV-vis diffuse reflectance spectra (DRS) of all samples is depicted in Fig. 7b. The light absorption edge of Fe_2O_3 is located at around 610 nm, which is close to 2.1 eV optical band gap (E_g) of pristine Fe_2O_3 [15,60]. After the deposition of CdS and Co-Pi respectively, both $\text{Fe}_2\text{O}_3/\text{CdS}$ and $\text{Fe}_2\text{O}_3/\text{Co-Pi}$ show enhanced UV and visible light absorption capability than the Fe_2O_3 . Noted that CdS and Co-Pi only deposits onto the surface and are unable to alter the crystal lattice of Fe_2O_3 , which has been confirmed by phase structure and morphology analysis. As a result, $\text{Fe}_2\text{O}_3/\text{CdS}$ and $\text{Fe}_2\text{O}_3/\text{Co-Pi}$ show the same E_g value as Fe_2O_3 .

Fig. 5. EDS spectra of the $\text{Fe}_2\text{O}_3/\text{CdS}/\text{Co-Pi}$ NRAs.

After depositing Co-Pi cocatalyst onto the surface of $\text{Fe}_2\text{O}_3/\text{CdS}$, the absorption edge of $\text{Fe}_2\text{O}_3/\text{CdS}/\text{Co-Pi}$ also does not change but the full spectrum absorption capability is enhanced. Due to the small amount of CdS and Co-Pi deposited, no light absorption edge shift occurred for all samples, while $\text{Fe}_2\text{O}_3/\text{CdS}/\text{Co-Pi}$ displays apparently enhanced light absorption capability than $\text{Fe}_2\text{O}_3/\text{CdS}$ and $\text{Fe}_2\text{O}_3/\text{Co-Pi}$, which should be attributed to the synergistic effect between CdS and Co-Pi that enhances the light absorption ability together. When applied in PEC water splitting process, Barroso and Klahr found that Co-Pi cocatalyst loaded on Fe_2O_3 anode would efficiently enhance the photocurrent, revealing the potential capability of such cocatalyst in PEC application [30,33]. In our work, higher charge transfer kinetics and lower onset potential have been achieved by the ternary $\text{Fe}_2\text{O}_3/\text{CdS}/\text{Co-Pi}$ compared to the binary ($\text{Fe}_2\text{O}_3/\text{CdS}$) and unitary (Fe_2O_3) counterparts. Such similar PEC improvement is also in accordance with the extended lifetime of photoinduced holes after depositing Co-Pi cocatalyst on the TiO_2 and TiO_2/CdS photoanodes [38,45]. The superior PEC performances of $\text{Fe}_2\text{O}_3/\text{CdS}/\text{Co-Pi}$ can be explained by the promoted charge separation and transfer efficiency as well as suppressed surface charge recombination.

3.4. PEC performance

The PEC performances of these Fe_2O_3 NRAs-based photoanodes were then evaluated in $1.0 \text{ M NaOH} + 0.1 \text{ M Na}_2\text{S}$ electrolyte. Fig. 8a presents the photocurrent-potential ($I-V$) characteristics of the pristine Fe_2O_3 , $\text{Fe}_2\text{O}_3/\text{CdS}$ and $\text{Fe}_2\text{O}_3/\text{CdS}/\text{Co-Pi}$ NRAs photoanodes under visible light illumination. Upon illumination, all

samples show the saturated photocurrent density. The pristine Fe_2O_3 exhibits a saturated photocurrent density of 1.05 mA cm^{-2} at high applied potential ($1.21 \text{ V}_{\text{RHE}}$), and $\text{Fe}_2\text{O}_3/\text{CdS}$ shows an enhanced saturated photocurrent density of 2.32 mA cm^{-2} at relative lower potential ($0.87 \text{ V}_{\text{RHE}}$). Dramatically, higher saturated photocurrent density of 3.29 mA cm^{-2} is obtained at much lower potential ($0.70 \text{ V}_{\text{RHE}}$) for $\text{Fe}_2\text{O}_3/\text{CdS}/\text{Co-Pi}$. To our knowledge, this is the impressive saturated photocurrent density over Fe_2O_3 photoanode in the presence of sacrificial agent. As for the continue rising of current density with increasing the applied potential, it should be ascribed to the dark current produced at high potential region. Noted that the photocurrent decrease of $\text{Fe}_2\text{O}_3/\text{CdS}$ after the saturated photocurrent should be ascribed to the excessive accumulation of holes on electrode surface, instead leads to the surface charge recombination and loss of effective photocurrent. It can be estimated that the $\text{Fe}_2\text{O}_3/\text{CdS}$ exhibits an onset potential of about $0.52 \text{ V}_{\text{RHE}}$, while the onset potential greatly negatively shifted to about $0.41 \text{ V}_{\text{RHE}}$ for $\text{Fe}_2\text{O}_3/\text{CdS}/\text{Co-Pi}$. The cathodic shifted onset potential could be due to the synergistic effect of CdS and Co-Pi, which eventually enhances the charge transfer kinetics and reduces the external applied voltage for generating photocurrent. More importantly, the increasing tendency of $I-V$ curves well demonstrates the efficient surface charge recombination of $\text{Fe}_2\text{O}_3/\text{CdS}/\text{Co-Pi}$ compared to that of $\text{Fe}_2\text{O}_3/\text{CdS}$ [61]. $\text{Fe}_2\text{O}_3/\text{CdS}/\text{Co-Pi}$ presents higher photocurrent value and larger increasing rate than that of the $\text{Fe}_2\text{O}_3/\text{CdS}$ in potential region from 0.4 to $0.6 \text{ V}_{\text{RHE}}$, suggesting the more efficient participation of charges in PEC process. In addition, the saturated photocurrent densities of $\text{Fe}_2\text{O}_3/\text{CdS}/\text{Co-Pi}$ NRAs and other promising photoan-

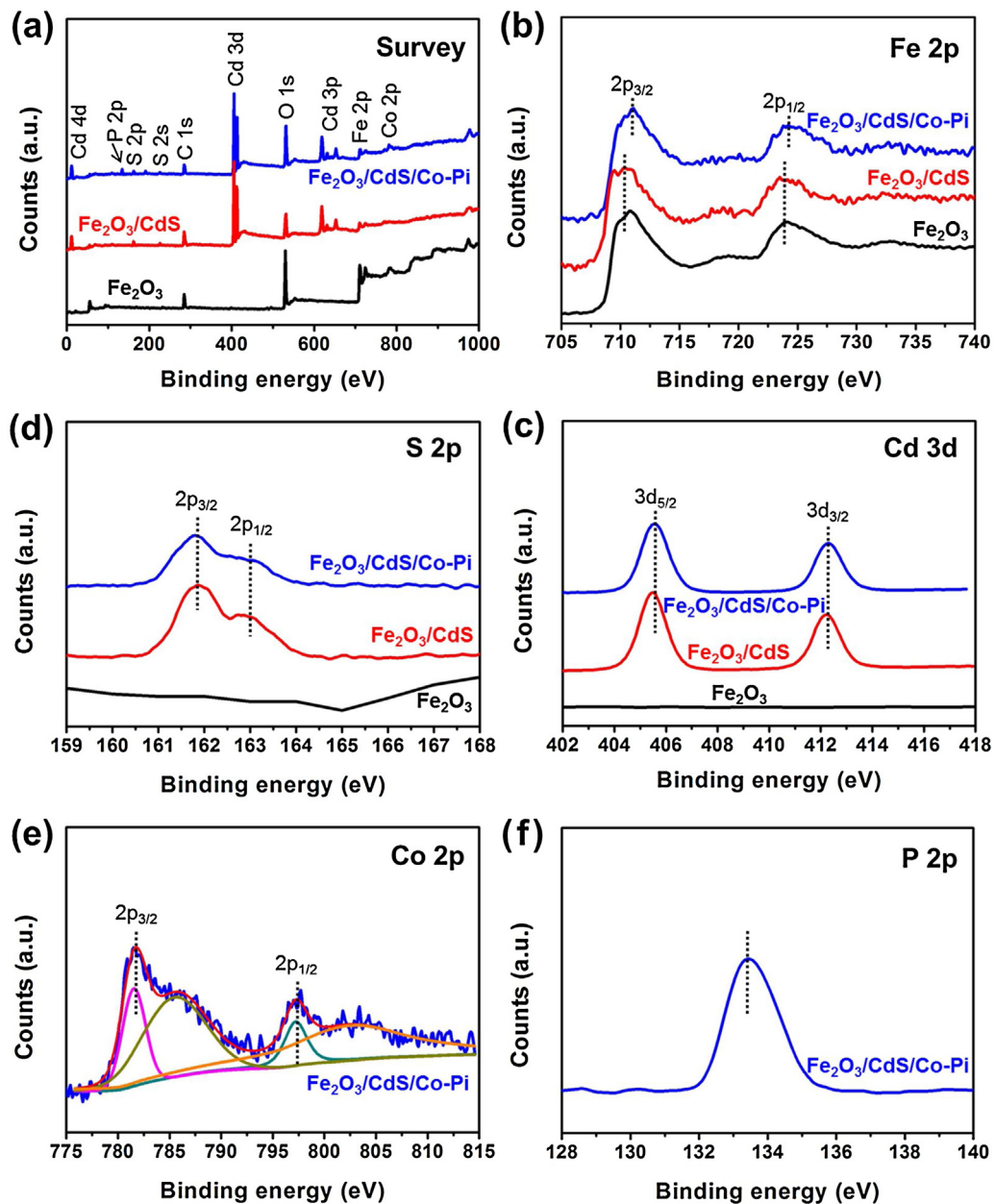


Fig. 6. XPS spectra of the samples: (a) Survey, (b) Fe 2p, (c) Cd 3d, (d) S 2p, (e) Co 2p and (f) P 2p.

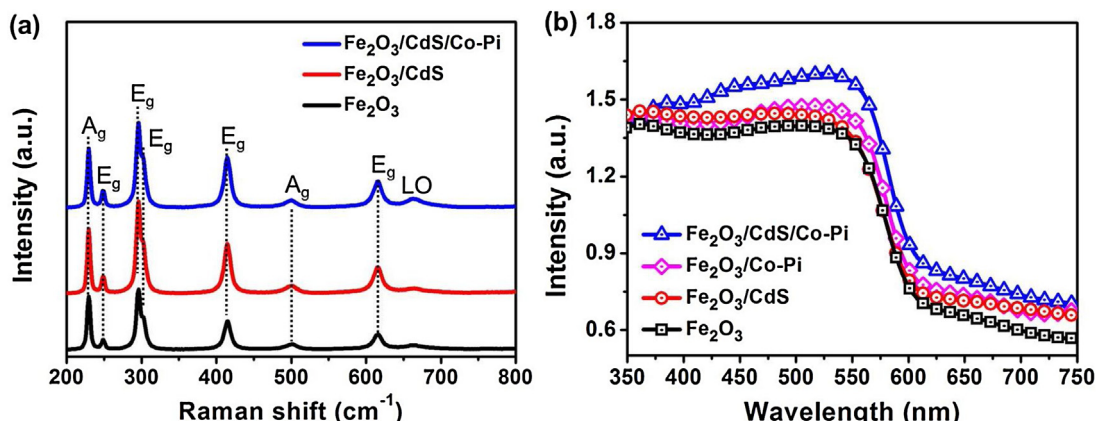


Fig. 7. (a) Raman and (b) DRS spectra of the Fe_2O_3 , $\text{Fe}_2\text{O}_3/\text{CdS}$ and $\text{Fe}_2\text{O}_3/\text{CdS}/\text{Co-Pi}$ NRAs photoanodes.

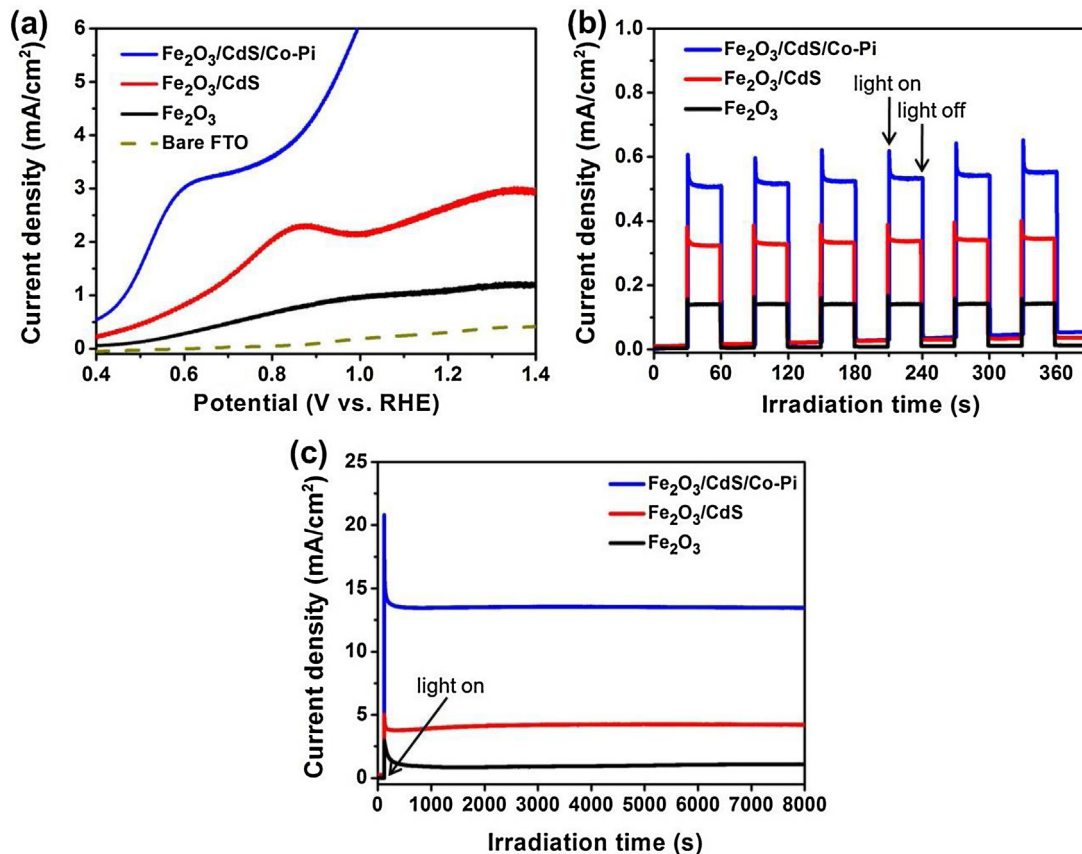


Fig. 8. PEC measurements of the prepared photoanodes. (a) *I*-*V* curves under visible light illumination, (b) *I*-*T* curves measured at open circuit voltage under chopped visible light illumination, and (c) steady-state photocurrent density curves under continuous visible light illumination with applied voltage of 1.4 V_{RHE}.

odes under light illumination in the presence of sacrificial agent are compared in Table S1. Our Fe₂O₃/CdS/Co-Pi NRAs case shows a much lower onset potential and significant enhancement of surface charge transfer kinetics. This is due to the introduction of CdS and Co-Pi that can not only effectively separate the charge carriers but also suppress surface recombination by slowing or blocking the back-flowed holes. To confirm the synergistic effect of CdS and Co-Pi, we also performed the *I*-*V* tests of Co-Pi modified Fe₂O₃ NRAs. Fig. S6 and S7 present the SEM, TEM images and *I*-*V* curves of Fe₂O₃/Co-Pi NRAs. It can be seen that Fe₂O₃/CdS/Co-Pi exhibits decreased onset potential and also enhanced photocurrent density at whole potential range compared to that of Fe₂O₃/CdS, Fe₂O₃/Co-Pi and pristine Fe₂O₃, clearly demonstrating the synergistic effect of CdS and Co-Pi.

Photocurrent-time (*I*-*T*) curves were measured at open circuit voltage under chopped light illumination for these photoanodes. As shown in Fig. 8b, the photocurrent rapidly increases under illumination and decreases to nearly zero at a similarly rapid rate when the light is blocked over several on-off cycles. The steady state photocurrent density of Fe₂O₃/CdS/Co-Pi (0.53 mA cm⁻²) is about 1.56 and 3.79 times higher than that of Fe₂O₃/CdS and Fe₂O₃, respectively, further demonstrating the enhanced charge separation and transfer efficiency after depositing CdS and Co-Pi. It is noted that the nearly vertical rise and fall of current density demonstrates the fast charge transfer in the photoanode. This tendency can be ascribed to the fast consumption of holes by Co-Pi cocatalyst as well as the direct and unhindered electron transfer channel created by the one-dimensional Fe₂O₃ NRAs structure. It is acknowledged that the photo illumination stability of electrode is indispensable for practical PEC application. Herein, the stability tests of these photoanodes were measured at 1.4 V_{RHE} for a continuous 2.2 h visible

light irradiation. As shown in Fig. 8c, prompt drop was occurred for photocurrent density within 15 min. Afterwards, the photocurrent densities of Fe₂O₃/CdS/Co-Pi, Fe₂O₃/CdS and Fe₂O₃ photoanodes reach a steady value. During the rest illumination process, no apparent decays of photocurrent density can be observed, which suggests the excellent stability of all of these prepared photoanodes.

3.5. M-S and EIS measurements

Mott-Schottky (M-S) plots were collected on Fe₂O₃-based photoanodes in dark condition in 1.0 M NaOH + 0.1 M Na₂S electrolyte. The conducting type and flat band potential (*V*_{fb}) of the samples can be calculated using the following equation [16]:

$$1/C^2 = (2/\varepsilon \varepsilon_0 e_0 N_d)[(V - V_{fb}) - kT/e_0] \quad (1)$$

where ε , ε_0 , e_0 and V represents the dielectric constant of semiconductor, permittivity of vacuum (8.854×10^{-12} F m⁻¹), electronic charge unit (1.602×10^{-19} C) and applied potential at the electrode, respectively. As shown in Fig. 9a, the positive slope of all samples manifests both Fe₂O₃ and CdS are n-type. By extrapolating, the *V*_{fb} of the Fe₂O₃, Fe₂O₃/CdS and Fe₂O₃/CdS/Co-Pi are determined to be around 0.43, 0.39 and 0.34 V_{RHE}. The *V*_{fb} of the electrode gradually shifts to negative potentials with the successive introduction of CdS and Co-Pi. These results further confirm the synergistic effect of CdS and Co-Pi in reducing surface passivation and promoting the reaction kinetics of Fe₂O₃ photoanode. Next, M-S curves slope is used to calculate the carrier density of samples [62]:

$$N_d = (2/\varepsilon \varepsilon_0 e_0)[d(1/C^2)/dV]^{-1}(2)$$

with an ε of 80 for Fe₂O₃ [63], the carrier densities of Fe₂O₃, Fe₂O₃/CdS and Fe₂O₃/CdS/Co-Pi are calculated to be 6.99×10^{19} ,

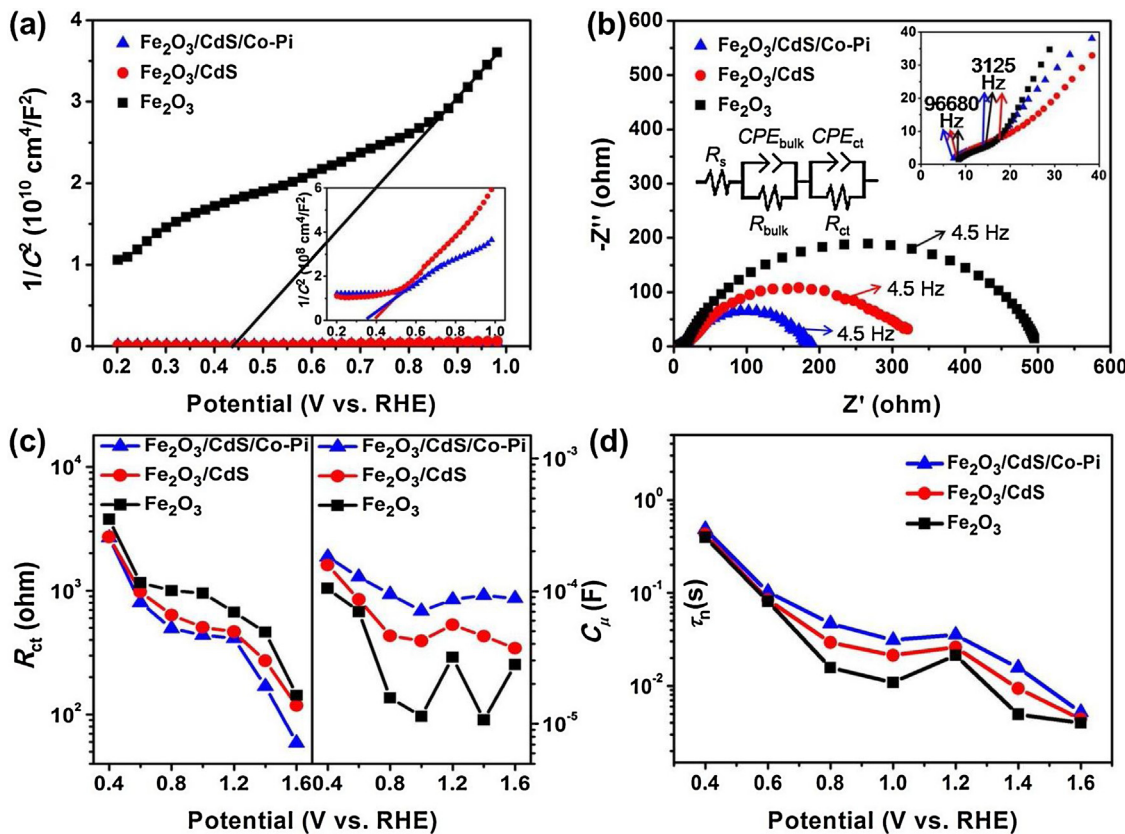


Fig. 9. (a) M-S plots of the Fe_2O_3 , $\text{Fe}_2\text{O}_3/\text{CdS}$ and $\text{Fe}_2\text{O}_3/\text{CdS}/\text{Co-Pi}$ NRAs photoanodes in dark at a frequency of 0.5 KHz and an amplitude of 5 mV, (b) EIS curves of the Fe_2O_3 , $\text{Fe}_2\text{O}_3/\text{CdS}$ and $\text{Fe}_2\text{O}_3/\text{CdS}/\text{Co-Pi}$ NRAs photoanodes under visible light illumination at $1.4 \text{ V}_{\text{RHE}}$, (c) interfacial charge transfer resistance R_{ct} and chemical capacitance C_{μ} extracted from the EIS spectra, and (d) calculated electron lifetime τ_n .

1.84×10^{21} and $2.71 \times 10^{21} \text{ cm}^{-3}$, respectively, which is comparable to the typical values of Fe_2O_3 [64]. To put the above comparisons on an obvious footing, the parameters are clearly listed in Table S2. The carrier density of $\text{Fe}_2\text{O}_3/\text{CdS}/\text{Co-Pi}$ is about two orders of magnitude higher than that of Fe_2O_3 , which should be attributed to the introduction of CdS and Co-Pi, resulting in more efficient charge separation and transfer, as well as reduced charge recombination within bulk and at the electrode/electrolyte interface. To be more specific, CdS increases the light absorption and charge separation efficiency, thus ameliorates the passive surface state of Fe_2O_3 . Meanwhile, Co-Pi has critical impact on facilitating the separated holes to participate in the irreversible oxidation reaction, which effectively promotes the charge transfer kinetics and inhibits the surface charge recombination. The result is similar to a recent work for Co-Pi modified TiO_2/CdS photoanode [45]. Therefore, the larger carrier density caused by enhanced surface reaction kinetics should be a cardinal factor for the superior PEC performances.

Fig. 9b shows the electrochemical impedance spectroscopy (EIS) plots of Fe_2O_3 , $\text{Fe}_2\text{O}_3/\text{CdS}$ and $\text{Fe}_2\text{O}_3/\text{CdS}/\text{Co-Pi}$ photoanodes carried out in $1.0 \text{ M NaOH} + 0.1 \text{ M Na}_2\text{S}$ electrolyte under visible light illumination at $1.4 \text{ V}_{\text{RHE}}$, and the inset gives the equivalent electric circuit fitting from EIS plots. Herein, R_s corresponds to the series resistance of the whole test system (start point 96680 Hz). The depressed semicircle at high frequency region (such as 3125 Hz) should be attributed to the electrochemical process within the electrode bulk, where the R_{bulk} and CPE_{bulk} represent the bulk charge trapping resistance and constant phase element that contains the bulk chemical capacitance, respectively [65,66]. Furthermore, the plump semicircle at low frequency region (such as 4.5 Hz) originates from the process at electrode/electrolyte interface, where the R_{ct} and CPE_{ct} symbolize the interfacial charge transfer resis-

tance and constant phase element that contains the interfacial chemical capacitance (C_{μ}), respectively [66,67]. Obviously, the $\text{Fe}_2\text{O}_3/\text{CdS}/\text{Co-Pi}$ shows much smaller semicircle than $\text{Fe}_2\text{O}_3/\text{CdS}$ and Fe_2O_3 at low frequency region, indicating decreased interfacial charge transfer resistance. In other words, Co-Pi cocatalyst greatly promotes the charge transfer kinetics, facilitates the transfer of separated holes across the electrode/electrolyte interface and thereby dramatically suppresses surface charge recombination. In addition, the typical characteristics such as R_{ct} and C_{μ} at electrode/electrolyte interface can be extracted from the EIS plots, which provides an insight into the phenomena occurring in the presence of the Co-Pi cocatalyst. As shown in Fig. 9c, R_{ct} and C_{μ} decreases with the increase of potentials for almost all the samples. In particular, the R_{ct} of $\text{Fe}_2\text{O}_3/\text{CdS}/\text{Co-Pi}$ is smaller than those of $\text{Fe}_2\text{O}_3/\text{CdS}$ and Fe_2O_3 in the whole potential region, suggesting the promotion of charge transfer kinetics at the electrode/electrolyte interface of $\text{Fe}_2\text{O}_3/\text{CdS}/\text{Co-Pi}$ photoanode. Reduced surface charge recombination will extend the electron lifetime (τ_n), which can be calculated by the expression $\tau_n = R_{\text{ct}}C_{\mu}$ [68]. As presented in Fig. 9d, τ_n decreases monotonically with increasing potentials. Due to the presence of Co-Pi cocatalyst, τ_n for $\text{Fe}_2\text{O}_3/\text{CdS}/\text{Co-Pi}$ exceeds that of $\text{Fe}_2\text{O}_3/\text{CdS}$ and Fe_2O_3 at all potentials. For instance, the τ_n value for $\text{Fe}_2\text{O}_3/\text{CdS}/\text{Co-Pi}$ at $1.4 \text{ V}_{\text{RHE}}$ is 15.7 ms, much higher than that of $\text{Fe}_2\text{O}_3/\text{CdS}$ (9.4 ms) and Fe_2O_3 (4.9 ms) under the same potential. For ease of comparison, the related parameters are extracted and listed in Table S3. The longer electron lifetime in $\text{Fe}_2\text{O}_3/\text{CdS}/\text{Co-Pi}$ indicates the remarkable suppression of the surface charge recombination at the electrode/electrolyte interface. As a consequence, more holes are able to participate in the reversible oxidation reaction on the electrode surface and simultaneously, more electrons

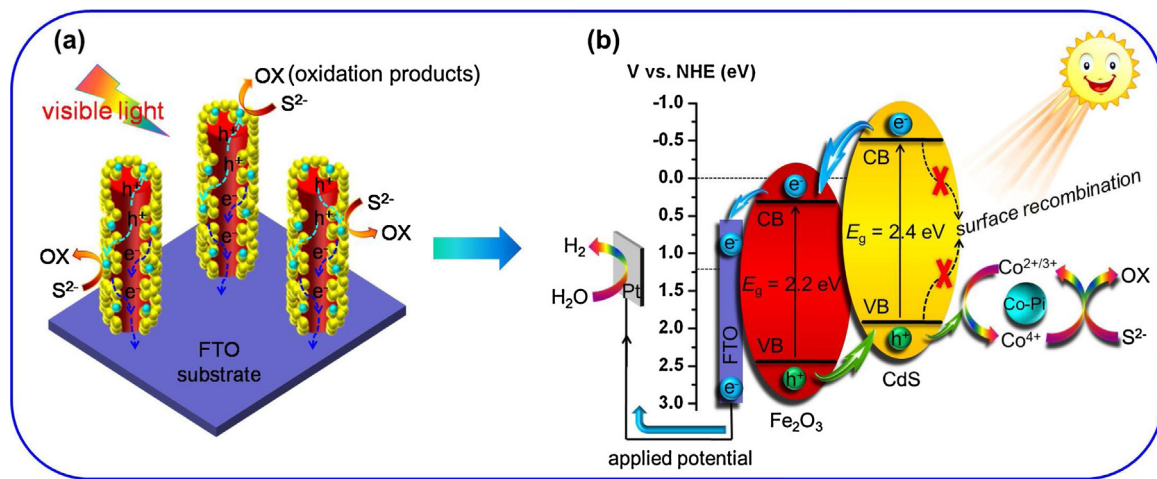


Fig. 10. Schematic diagram of (a) the proposed photoinduced electron-hole pairs separation and transfer trails and (b) band gap structures and kinetic active processes in Fe₂O₃/CdS/Co-Pi.

can be transferred to the counter electrode through the external circuit, resulting in enhanced PEC performances (Fig. 10a).

According to above analysis on PEC performances, M-S curves and EIS plots, it is assumed that Co-Pi cocatalyst has played a significant role in the photoinduced holes transfer process at electrode/electrolyte interface, i.e., enhancing the charge transfer kinetics and reducing the surface charge recombination. To verify this proposition, Bode plots are obtained at different potentials and presented in Fig. S8. Each peak of the plots can be related to a certain control process of electrode. The higher the peak, the more dominant control of the corresponding process [66]. It can be seen that the higher peaks of all samples are dominant by low frequency at all potentials, suggests that the charge transfer process at electrode/electrolyte interface is the decisive step in PEC measurements. This analysis proves the above hypothesis that Co-Pi cocatalyst greatly suppresses the surface charge recombination and promotes the reaction kinetics Fe₂O₃/CdS/Co-Pi.

3.6. Proposed mechanism

The mechanism for improved PEC activities by synergistic effect of Co-Pi and CdS can be summarized, and the primary function of Co-Pi cocatalyst in this ternary composite material can now be comprehended. When irradiated by visible light, pristine Fe₂O₃ could generate photoinduced electron-hole pairs, but these pairs are much easier to recombine within bulk and at surface due to its sluggish reaction kinetics. Although easy to be excited by visible light, however, Fe₂O₃ is known to be a self-limiting semiconductor on which the positive surface charge (photoinduced holes) accumulation inevitably restrains band bending through quasi-Fermi Level pinning, leading to the fast charge recombination [31,69]. Furthermore, photoinduced electrons from Fe₂O₃ far away from FTO substrate could quickly recombine with holes before they can be timely transferred to the external circuit because of the intrinsic low conductivity, low mobility and short electron diffusion length of Fe₂O₃ [69]. After depositing appropriate CdS onto Fe₂O₃, the photoinduced electron-hole pairs could be effectively separated at Fe₂O₃/CdS interface because of the formed type-II band gap structure that directly injects the electrons and holes into two different semiconductors, respectively [49]. Therefore, CdS efficiently eliminate the native charge recombination of Fe₂O₃, allowing it to behave in a more ideal pathway, where valence band holes and conduction band electrons are only transferred to CdS and Fe₂O₃, respectively. But even so, holes accumulated on CdS valence band will suffer greatly from the serious surface charge recombination

over CdS due to the low consuming rate of holes with sacrificial agent (Fig. S9), thus, leads to the “kinetic bottleneck” phenomenon over Fe₂O₃/CdS. Hence, the surface recombination is a primary loss pathway for charges and leads to poor charge transfer kinetics, especially at low applied potentials. After depositing Co-Pi cocatalyst on Fe₂O₃/CdS, the charge transfer kinetics is greatly promoted and surface charge recombination is indeed suppressed. Moreover, much lower onset potential is required to produce photocurrent for Fe₂O₃/CdS/Co-Pi than that of the Fe₂O₃/CdS. After Co-Pi cocatalyst modification, photoinduced holes transfer to Fe₂O₃/CdS surface and then collected by Co-Pi, meanwhile, the photoinduced electrons transfer to the external circuit under the applied potential, which ultimately greatly decreases the surface holes accumulation and charge recombination (Fig. 10b). In general, the function of Co-Pi cocatalyst is to tune the balance between charge transfer kinetics and surface charge recombination [31]. In our case, after introducing Co-Pi cocatalyst, charge transfer kinetics and holes consumption are competitive against native surface charge recombination. Except the synergistic effect of CdS and Co-Pi, Fe₂O₃ NRAs serve as efficient electron transport channels to accelerate the transportation of separated electrons to the FTO substrate and external circuit, which also contributes to the enhanced charge transfer kinetics. The combination of these two advantages synergistically results in much more facile PEC performances, and makes the desired catalysis kinetically competitive with energy-wasting surface charge recombination process.

4. Conclusions

In summary, we have designed and fabricated an innovative ternary thrice coating photoanode Fe₂O₃/CdS/Co-Pi comprising vertically aligned Fe₂O₃ NRAs, narrow band gap and visible light responsive CdS and efficient charge transfer medium of Co-Pi cocatalyst for PEC water splitting application. As expected, sluggish surface kinetics of Fe₂O₃ is greatly ameliorated upon deposition of CdS and Co-Pi, which is reflected in the increasing in charge transfer kinetics and decreasing in onset potential. In addition, due to the deposition of Co-Pi cocatalyst, electrode/electrolyte interface charge transfer resistance has been greatly reduced. Thus, photoinduced holes could inject into electrolyte more efficiently, which reduces the surface charge recombination even more, and contributes to the excellent stability and increased carrier density. Moreover, the type-II band structure of Fe₂O₃/CdS and one-dimensional morphology of Fe₂O₃ NRAs provide a continuous channel for fast charge separation and transfer, thus enhancing

charge separation efficiency. The synergistic effect of CdS and Co-Pi achieves rapid charge transfer kinetics and low positive potential to produce photocurrent. This work has exhibited the advantages of $\text{Fe}_2\text{O}_3/\text{CdS}/\text{Co-Pi}$ NRAs photoanode, and the remarkable performances indicate the potential PEC application and other electronic nanodevices.

Acknowledgements

This study was partially supported by National Basic Research Program of China (2013CB632402), NSFC (51320105001, 51372190, 21433007 and 21573170). Also, this work was financially supported by the Natural Science Foundation of Hubei Province of China (2015CFA001), the Fundamental Research Funds for the Central Universities (WUT: 2015-III-034) and Innovative Research Funds of SKLWUT (2017-ZD-4).

Appendix A. Supplementary data

Supplementary data associated with this article can be found, in the online version, at <http://dx.doi.org/10.1016/j.apcatb.2017.07.002>.

References

- [1] H.M. Chen, C.K. Chen, R.S. Liu, L. Zhang, J. Zhang, D.P. Wilkinson, *Chem. Soc. Rev.* 41 (2012) 5654–5671.
- [2] P.V. Kamat, K. Tvrdy, D.R. Baker, J.G. Radich, *Chem. Rev.* 110 (2010) 6664–6688.
- [3] Y. Zhang, H. Zhang, H. Ji, W. Ma, C. Chen, J. Zhao, *J. Am. Chem. Soc.* 138 (2016) 2705–2711.
- [4] G. Iervolino, I. Tantis, L. Sygellou, V. Vaiano, D. Sannino, P. Lianos, *Appl. Surf. Sci.* 400 (2017) 176–183.
- [5] Y.F. Xu, H.S. Rao, X.D. Wang, H.Y. Chen, D.B. Kuang, C.Y. Su, *J. Mater. Chem. A* 4 (2016) 5124–5129.
- [6] P.Y. Kuang, J.R. Ran, Z.Q. Liu, H.J. Wang, N. Li, Y.Z. Su, Y.G. Jin, S.Z. Qiao, *J. Chem. Eur.* 21 (2015) 15360–15368.
- [7] Q. Wang, N. Zhu, E. Liu, C. Zhang, J.C. Crittenden, Y. Zhang, Y. Cong, *Appl. Catal. B: Environ.* 205 (2017) 347–356.
- [8] X. Zhang, B. Zhang, Y. Luo, X. Lv, Y. Shen, *Appl. Surf. Sci.* 391 (2017) 288–294.
- [9] L. Xia, J. Bai, J. Li, Q. Zeng, L. Li, B. Zhou, *Appl. Catal. B: Environ.* 204 (2017) 127–133.
- [10] K. Trzciński, M. Szkoda, K. Siuzdak, M. Sawczak, A. Lisowska-Oleksiak, *Appl. Surf. Sci.* 388 (2016) 753–761.
- [11] Y. Yuan, J. Gu, K.H. Ye, Z. Chai, X. Yu, X. Chen, C. Zhao, Y. Zhang, W. Mai, *ACS Appl. Mater. Interfaces* 8 (2016) 16071–16077.
- [12] Y. Hou, C. Zheng, Z. Zhu, X. Wang, *Chem. Commun.* 52 (2016) 6888–6891.
- [13] M. Einert, R. Ostermann, T. Weller, S. Zellmer, G. Garnweitner, B.M. Smarsly, R. Marschall, *J. Mater. Chem. A* 4 (2016) 18444–18456.
- [14] G. Wang, Y. Ling, D.A. Wheeler, K.E. George, K. Horsley, C. Heske, J.Z. Zhang, Y. Li, *Nano Lett.* 11 (2011) 3503–3509.
- [15] X.M. Song, X. Zhou, C. Yuan, Y. Zhang, Q. Tong, Y. Li, L. Cui, D. Liu, W. Zhang, *Appl. Surf. Sci.* 397 (2017) 112–118.
- [16] R. Franking, L. Li, M.A. Lukowski, F. Meng, Y. Tan, R.J. Hamers, S. Jin, *Energy Environ. Sci.* 6 (2013) 500–512.
- [17] Y.W. Phuan, E. Ibrahim, M.N. Chong, T. Zhu, B.K. Lee, J.D. Ocon, E.S. Chan, *Appl. Surf. Sci.* 392 (2017) 144–152.
- [18] L. Qin, M. Liu, Y. Wu, Z. Xu, X. Guo, G. Zhang, *Appl. Catal. B: Environ.* 194 (2016) 50–60.
- [19] M. Li, Y. Yang, Y. Ling, W. Qiu, F. Wang, T. Liu, Y. Song, X. Liu, P. Fang, Y. Tong, Y. Li, *Nano Lett.* 17 (2017) 2490–2495.
- [20] Y. Ling, G. Wang, H. Wang, Y. Yang, Y. Li, *ChemSusChem* 7 (2014) 848–853.
- [21] K. Zhao, X. Yan, Y. Gu, Z. Kang, Z. Bai, S. Cao, Y. Liu, X. Zhang, Y. Zhang, *Small* 12 (2016) 245–251.
- [22] J. Li, S.K. Cushing, P. Zheng, T. Senty, F. Meng, A.D. Bristow, A. Manivannan, N. Wu, *J. Am. Chem. Soc.* 136 (2014) 8438–8449.
- [23] R. Pan, Y. Wu, Z. Li, Z. Fang, *Appl. Surf. Sci.* 292 (2014) 886–891.
- [24] A. Boonserm, C. Kruehong, V. Seithantanabutara, A. Artnaseaw, P. Kwakhong, *Appl. Surf. Sci.* 419 (2017) 933–941.
- [25] C. Eley, T. Li, F. Liao, S.M. Fairclough, J.M. Smith, G. Smith, S.C. Tsang, *Angew. Chem. Int. Ed.* 53 (2014) 7838–7842.
- [26] T.C. Kaspar, D.K. Schreiber, S.R. Spurgeon, M.E. McBriarty, G.M. Carroll, D.R. Gamelin, S.A. Chambers, *Adv. Mater.* 28 (2016) 1616–1622.
- [27] Y. Shi, H. Li, L. Wang, W. Shen, H. Chen, *ACS Appl. Mater. Interfaces* 4 (2012) 4800–4806.
- [28] S. Zhang, W. Xu, M. Zeng, J. Li, J. Xu, X. Wang, *Dalton Trans.* 42 (2013) 13417–13424.
- [29] A.J. Cowan, J.R. Durrant, *Chem. Soc. Rev.* 42 (2013) 2281–2293.
- [30] B. Klahr, S. Gimenez, F. Fabregat-Santiago, J. Bisquert, T.W. Hamann, *J. Am. Chem. Soc.* 134 (2012) 16693–16700.
- [31] G.M. Carroll, D.R. Gamelin, *J. Mater. Chem. A* 4 (2016) 2986–2994.
- [32] M. Barroso, S.R. Pendlebury, A.J. Cowan, J.R. Durrant, *Chem. Sci.* 4 (2013) 2724–2734.
- [33] M. Barroso, A.J. Cowan, S.R. Pendlebury, M. Gratzel, D.R. Klug, J.R. Durrant, *J. Am. Chem. Soc.* 133 (2011) 14868–14871.
- [34] C.C. McCrory, S. Jung, I.M. Ferrer, S.M. Chatman, J.C. Peters, T.F. Jaramillo, *J. Am. Chem. Soc.* 137 (2015) 4347–4357.
- [35] G.M. Carroll, D.K. Zhong, D.R. Gamelin, *Energy Environ. Sci.* 8 (2015) 577–584.
- [36] Y. Li, T. Takata, D. Cha, K. Takanabe, T. Minegishi, J. Kubota, K. Domen, *Adv. Mater.* 25 (2013) 125–131.
- [37] E.S. Kim, N. Nishimura, G. Magesh, J.Y. Kim, J.W. Jang, H. Jun, J. Kubota, K. Domen, J.S. Lee, *J. Am. Chem. Soc.* 135 (2013) 5375–5383.
- [38] G. Ai, R. Mo, H. Li, J. Zhong, *Nanoscale* 7 (2015) 6722–6728.
- [39] H. Ye, H.S. Park, A.J. Bard, *J. Phys. Chem. C* 115 (2011) 12464–12470.
- [40] T. Di, B. Zhu, J. Zhang, B. Cheng, J. Yu, *Appl. Surf. Sci.* 389 (2016) 775–782.
- [41] H. Meng, K. Fan, J. Low, J. Yu, *Dalton Trans.* 45 (2016) 13717–13725.
- [42] Z. He, J. Fu, B. Cheng, J. Yu, S. Cao, *Appl. Catal. B: Environ.* 205 (2017) 104–111.
- [43] K. Fan, F. Li, L. Wang, Q. Daniel, H. Chen, E. Gabrielsson, J. Sun, L. Sun, *ChemSusChem* 8 (2015) 3242–3247.
- [44] L. Ge, C. Han, X. Xiao, L. Guo, *Appl. Catal. B: Environ.* 142–143 (2013) 414–422.
- [45] G. Ai, H. Li, S. Liu, R. Mo, J. Zhong, *Adv. Funct. Mater.* 25 (2015) 5706–5713.
- [46] Y. Li, R. Wang, H. Li, X. Wei, J. Feng, K. Liu, Y. Dang, A. Zhou, *J. Phys. Chem. C* 119 (2015) 20283–20292.
- [47] J. Zhang, J. Yu, M. Jaroniec, J.R. Gong, *Nano Lett.* 12 (2012) 4584–4589.
- [48] A. Meng, B. Zhu, B. Zhong, L. Zhang, B. Cheng, *Appl. Surf. Sci.* 422 (2017) 518–527.
- [49] P.Y. Kuang, Y.Z. Su, K. Xiao, Z.Q. Liu, N. Li, H.J. Wang, J. Zhang, *ACS Appl. Mater. Interfaces* 7 (2015) 16387–16394.
- [50] P.Y. Kuang, P.X. Zheng, Z.Q. Liu, J.L. Lei, H. Wu, N. Li, T.Y. Ma, *Small* 12 (2016) 6735–6744.
- [51] M. Shao, F. Ning, M. Wei, D.G. Evans, X. Duan, *Adv. Funct. Mater.* 24 (2014) 580–586.
- [52] K.J. McDonald, K.S. Choi, *Chem. Mater.* 23 (2011) 1686–1693.
- [53] D. Wang, R. Li, J. Zhu, J. Shi, J. Han, X. Zong, C. Li, *J. Phys. Chem. C* 116 (2012) 5082–5089.
- [54] S. Haschke, Y. Wu, M. Bashouti, S. Christiansen, J. Bachmann, *ChemCatChem* 7 (2015) 2455–2459.
- [55] Z.Q. Liu, P.Y. Kuang, R.B. Wei, N. Li, Y.B. Chen, Y.Z. Su, *RSC Adv.* 6 (2016) 16122–16130.
- [56] G.D. Khattak, A. Mekki, M.A. Gondal, *J. Phys. Chem. Solids* 74 (2013) 13–17.
- [57] N. Mirbagheri, D. Wang, C. Peng, J. Wang, Q. Huang, C. Fan, E.E. Ferapontova, *ACS Catal.* 4 (2014) 2006–2015.
- [58] Y. Ling, G. Wang, J. Reddy, C. Wang, J.Z. Zhang, Y. Li, *Angew. Chem. Int. Ed.* 51 (2012) 4074–4079.
- [59] X. Li, P.S. Bassi, P.P. Boix, Y. Fang, L.H. Wong, *ACS Appl. Mater. Interfaces* 7 (2015) 16960–16966.
- [60] L. Chen, F. He, N. Zhao, R. Guo, *Appl. Surf. Sci.* 420 (2017) 669–680.
- [61] Q. Liu, F. Cao, F. Wu, H. Lu, L. Li, *Adv. Mater. Interfaces* 3 (2016) 1600256.
- [62] P.Y. Kuang, Y.Z. Su, G.F. Chen, Z. Luo, S.Y. Xing, N. Li, Z.Q. Liu, *Appl. Surf. Sci.* 358 (2015) 296–303.
- [63] A. Pu, J. Deng, M. Li, J. Gao, H. Zhang, Y. Hao, J. Zhong, X. Sun, *J. Mater. Chem. A* 2 (2014) 2491–2497.
- [64] X. Qi, G. She, X. Huang, T. Zhang, H. Wang, L. Mu, W. Shi, *Nanoscale* 6 (2014) 3182–3189.
- [65] Z. Hu, Z. Shen, J.C. Yu, *Chem. Mater.* 28 (2016) 564–572.
- [66] F. Malaria, A. Minguzzi, M. Marelli, S. Morandi, R. Psaro, V. Dal Santo, A. Naldoni, *ACS Catal.* 5 (2015) 5292–5300.
- [67] K. Shimizu, J.F. Boily, *Langmuir* 30 (2014) 9591–9598.
- [68] Z. Yang, S. Gao, T. Li, F.Q. Liu, Y. Ren, T. Xu, *ACS Appl. Mater. Interfaces* 4 (2012) 4419–4427.
- [69] L. Li, Y. Yu, F. Meng, Y. Tan, R.J. Hamers, S. Jin, *Nano Lett.* 12 (2012) 724–731.